Research Square

Preprints are preliminary reports that have not undergone peer review.
They should not be considered conclusive, used to inform clinical practice,
or referenced by the media as validated information.

Single-molecule neuromorphic device

Wenjing Hong

whong@xmu.edu.cn

Xiamen University https://orcid.org/0000-0003-4080-6175

Hua Zhang

Xiamen University

Jingyao Ye

Xiamen University

Mingbin Gao

Xiamen University https://orcid.org/0000-0002-7143-2658

Chenshuai Yan

Xiamen University

Yiqiang Jiang

Xiamen University

Bei Zhang

Xiamen University

Yu Zhou

Xiamen University

Wansong Shang

Institute of Chemistry, Chinese Academy of Sciences

Liangliang Chen

Institute of Chemistry, Chinese Academy of Sciences

Jiayi Wu

Xiamen University

Wei Xu

Xiamen University

Xiaohui Li

Xiamen University

Jie Bai

Xiamen University

Jing Li

Xiamen University

Yanxi Zhang

Xiamen University

Zongyuan Xiao
Xiamen University
Jia Shi
State Key Laboratory of Physical Chemistry of Solid Surfaces, iChEM, Xiamen University
Guanxin Zhang
Institute of Chemistry,Chinese Academy of Sciences https://orcid.org/0000-0002-1417-6985
Junyang Liu
Xiamen University https://orcid.org/0000-0002-7252-1900
Deqing Zhang
Institute of Chemistry, Chinese Academy of Sciences https://orcid.org/0000-0002-5709-6088

Article

Keywords:

Posted Date: November 11th, 2025

DOI: https://doi.org/10.21203/rs.3.rs-7679516/v1

License: This work is licensed under a Creative Commons Attribution 4.0 International License.
Read Full License

Additional Declarations: There is **NO** Competing Interest.

Version of Record: A version of this preprint was published at Nature Communications on March 31st, 2026. See the published version at https://doi.org/10.1038/s41467-026-71127-2.

Single-molecule neuromorphic device

Hua Zhang[1,2,3]†, Jingyao Ye[1]†, Mingbin Gao[1]†, Chenshuai Yan[1], Yiqiang Jiang[1], Bei Zhang[1], Yu Zhou[1], Wansong Shang[2,3], Liangliang Chen[2,3], Jiayi Wu[1], Wei Xu[1], Xiaohui Li[1], Jie Bai[1], Jing Li[1], Yanxi Zhang[1], Zongyuan Xiao[1], Jia Shi[1], Guanxin Zhang[2,3], Junyang Liu[1]*, Deqing Zhang[2,3]*, Wenjing Hong[1]*

[1]State Key Laboratory of Physical Chemistry of Solid Surfaces, College of Chemistry and Chemical Engineering & Institute of Artificial Intelligence & IKKEM, Xiamen University, Xiamen, 361005, China.
[2]Beijing National Laboratory for Molecular Sciences, Organic Solids Laboratory, Institute of Chemistry, Chinese Academy of Sciences, Beijing 100190, China.
[3]School of Chemical Sciences, University of Chinese Academy of Sciences, Beijing 100049, China.
†These authors contributed equally.
*Corresponding authors.
E-mail: whong@xmu.edu.cn (W. Hong); dqzhang@iccas.ac.cn (D. Zhang); jyliu@xmu.edu.cn (J. Liu)

Abstract: Artificial neural network-based machine learning provides foundations for artificial intelligence (AI), yet requires high energy costs for training. Beyond software-level simulation of neural networks, hardware-level implementation via neuromorphic devices becomes the next milestone in nanoscience towards energy-sustainable AI. Single-molecule devices have the potential for ultimate scale and energy efficiency, but challenges remain in achieving programmable multi-conductance states amidst room-temperature thermal fluctuations. Here we fabricate a bio-inspired single-molecule neuromorphic device consuming ~2.8 aJ/operation by electrochemically gating molecule-ion electrostatic interactions. This device realizes biomimetic emulation of neural plasticity from short-term to long-term memory featuring over 10 distinct conductance states, demonstrating the applications in Pavlovian conditioning for associative learning and pattern recognition in Morse code processing. Our approach enables multi-state synaptic emulation using an individual molecule toward energy-sustainable AI.

Main

Large-scale neural networks, such as GPT-4 with trillions of artificial neurons, have demonstrated great promise for artificial intelligence (AI) but also consumed large amounts of energy for the training of these networks[1,2]. To address the exponentially growing energy demands of AI, inspired by the energy-efficient operations from biological neural systems, neuromorphic computing[3-7] has demonstrated the potential for the hardware-level simulation of neural networks, employing diverse materials from silicon-based semiconductors to organic electrochemical transistors[8-10]. Long-term efforts to reduce operating energy have made substantial progress through the evolution from HP's memristor[11] to current state-of-the-art inorganic[12,13] and

organic[14] devices, but the most advanced transistors still consume ~240 aJ (10^{-18} J) per operation[15]. As neuromorphic devices at the ultimate scale, single-molecule neuromorphic devices represent a promising solution with potential energy consumption of several aJ per operation, leveraging their atomic-scale dimensions and electron tunneling mechanisms with low inter-state energy barriers[16-22].

Molecular materials have demonstrated potential for neuromorphic computing due to their unique tunable band structures and multiple conductance states with high energy efficiency[23]. To further minimize channel length, self-assembled monolayers (SAMs)[24,25] with ~2 nm thickness have been employed to implement neuromorphic functions but still more than thousands of molecules involved in the switching, and then single fullerene within ~1 nm length was used to achieve logic operations[26-28] through external electric field-induced dipole inversion. However, current state-of-the-art single-fullerene logic-in-memory devices remain limited to two conductance states due to the restricted number of thermodynamically stable conformations at room temperature[29-31]. Drawing inspiration of the ion channel dynamics from biological synapses, recent advances in elegantly controlling electrostatic molecule-ion interactions at the single-molecule scale offer a promising approach to fix the molecular conformations,[32-34] thereby enabling multiple non-volatile conductance states with minimal energy consumption.

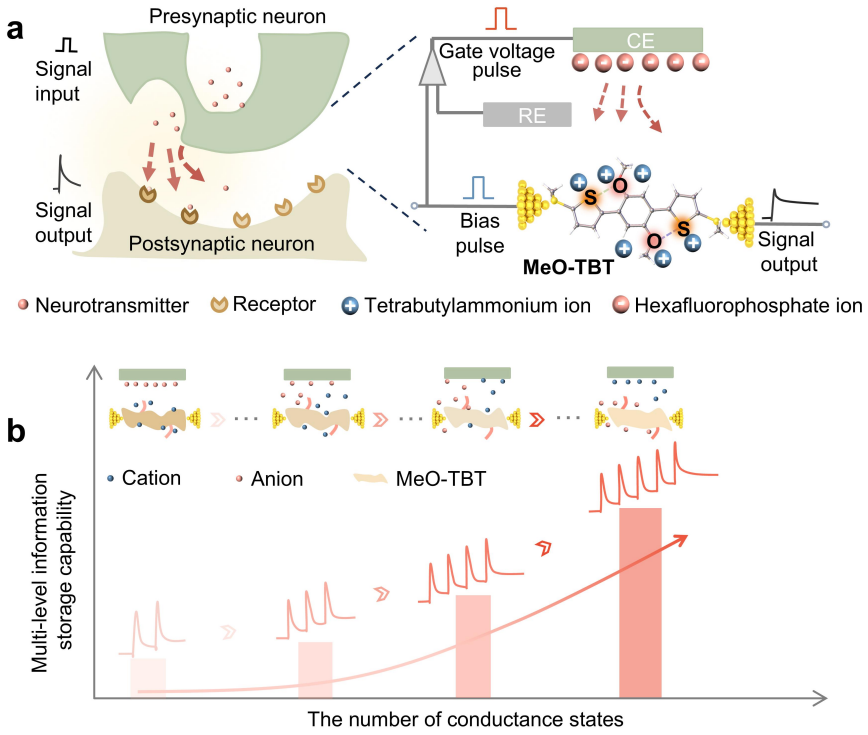


Fig. 1 Single-molecule neuromorphic device. a, Comparison between a biological synapse (left) and the artificial single-molecule neuromorphic device (right). **b,** Scaling of information processing and storage capacity with numbers of non-volatile conductance states.

Here we fabricated single-molecule neuromorphic devices by modulating electrostatic coupling between a single 5,5'-(2,5-dimethoxy-1,4-phenylene) bis(2-(methylthio)thiophene) (**MeO-TBT**) molecule and tetrabutylammonium cations (TBA^+) (Fig. 1a) using electrochemical scanning tunneling microscopy break junction (EC-STMBJ) techniques[35-40]. Through synchronized application of a bias pulse (reducing the dihedral thiophenyl-phenyl angle in **MeO-TBT** molecule) and a gate voltage pulse (driving TBA^+ to disrupt the S-O interactions for tuning the dihedral angle in **MeO-TBT** molecule)[41], we achieved an operation energy consumption of ~2.8 aJ, six orders of magnitude lower than that of a conventional 2-CMOS-transistor neuron implementation (~415 pJ)[42]. By controlling molecule-cation interactions (Fig. 1b), the device emulates both short-term plasticity (STP) with 307.99% paired-pulse facilitation and long-term synaptic plasticity (LTP) featuring over 10 non-volatile conductance states, thereby performing associative learning through Pavlovian conditioning while enabling recognitions of Morse code and handwritten digits. Theoretical calculations reveal that the averaged energy consumption of displacing TBA^+ cations reaches ~2.1 aJ per cation, thus inducing multiple conductance states through varying degrees of conformational locking by S-O interactions.

Emulating synaptic plasticity in a single-molecule neuromorphic device

Inspired by ion-mediated biological information processing, we demonstrate dynamic modulation of molecular junction transport properties through electrostatic coupling/decoupling between **MeO-TBT** molecules and cations, emulating synaptic multi-conductance behavior (Fig. 2a). Initially at V_G = –0.4 V (vs. Ag/AgCl), cations migrate to the junction under the applied field and form electrostatic couplings that disrupt molecular planarity through S-O interaction breaking, establishing a low-conductance state (**State I**). Subsequent application of a positive gate voltage pulse (**State II**) drives cations away from the junction (**State III**), weakening coupling effects and restoring molecular planarity. This enhances π-electron delocalization to increase conductance. Upon pulse removal (**State IV**), ion diffusion returns the system to equilibrium while the conductance gradually decays to its initial value, replicating synaptic plasticity. Experimental results confirm gate-voltage-dependent conductance modulation (Figs. S1-6), consistent with the predicted molecule-ion coupling behavior.

To investigate the neuromorphic functionality of our single-molecule device, we analyzed its current-gate voltage (I-V_G) characteristics and observed pronounced hysteresis effects (Fig. 2b and Figs. S7-10). The device emulated excitatory postsynaptic conductance (EPSC) through single gate-voltage pulses. At 1 mV bias with 1 ms pulse width, it demonstrated ultra-low energy consumption averaging ~2.8 aJ per synaptic event, while the minimum operation energy reaching ~0.8 aJ (blue curve in Fig. 2b). Statistical analysis of operational energy consumption across different bias voltages (1, 10, and 100 mV; Fig. 2b inset) revealed a voltage-dependent trend. Gaussian fitting of over 100 independent measurements showed the per-operation energy increasing from 2.8 aJ to 229.4 fJ with applied

voltage. Fig. 2c presents a comprehensive benchmarking framework that compares channel length versus energy consumption. Current technologies exhibit a fundamental trade-off, as monolayer devices achieve sub-nm channels but require μJ-level energy, whereas carbon nanotube devices reach aJ-level consumption with μm-scale dimensions. The dashed lines indicate theoretical projections for Si CMOS and NEMS devices (Table S1) provided by International Roadmaps for Devices and Systems (IRDS)[43,44]. Remarkably, our device achieves breakthroughs on both axes, attaining sub-nanometer channel dimensions (*X*-axis) and aJ-level energy consumption (*Y*-axis), thereby demonstrating advantages of miniaturization and low-power operation.

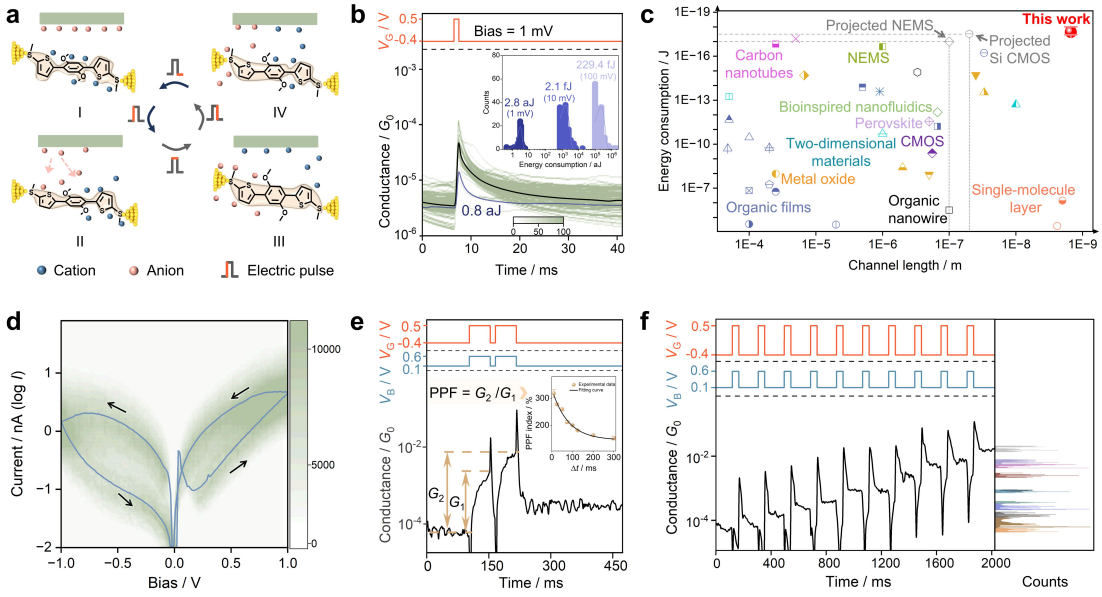


Fig. 2 Synaptic plasticity emulation in a single-molecule neuromorphic device. a, Schematic of ion redistribution in the **MeO-TBT**-based molecular transistor under electrical stimulation. **b,** Conductance statistics (105 traces) under single V_G pulses (–0.4 to 0.5 V) at V_B = 1 mV, with black curve showing the fitted trend (inset). Energy consumption comparisons at V_B = 1, 10, and 100 mV are shown (inset), where the blue curve represents experimental data. **c,** Benchmarking of published neuromorphic devices by channel length versus energy consumption (see Supplementary Information). **d,** *I*-V_B characteristics (2184 traces) and fitting (blue line) for forward and reverse scans at V_G = –0.4 V, using 0.5 mM **MeO-TBT** in 0.2 M solution of tetrabutylammonium hexafluorophosphate ($TBAPF_6$) in propylene carbonate (PC). **e,** Paired-pulse facilitation (PPF) under combined V_G = 0.5 V and V_B = 0.6 V pulses (t_p = 50 ms, Δt = 10 ms; 1 G_0 = 77.5 μS). Inset shows PPF index (G_2 /G_1) for Δt = 10-300 ms. Error bars present standard deviation of at least three measurements of the same device. **f,** Long-term plasticity and multiple conductance (right histograms) achieved with combined stimulation of gate voltage pulses and bias voltage pulses (V_G = 0.5 V, V_B = 0.6 V, t_p= 50 ms, Δt = 150 ms).

Further, exclusively driven by gate voltage pulses, the device demonstrates a bias-voltage-dependent transition from volatile to nonvolatile behavior. Current-bias voltage (I-V_B) statistical analysis further reveals distinct hysteresis effects (Fig. 2d and Figs. S8, S9, S11). By optimizing experimental conditions with synchronized gate and bias voltage pulses at a low operating voltage of 0.1 V, we achieved enhanced device non-volatility through synergistic electrical stimulation (Figs. S12-17). This configuration enabled EPSC emulation across varying pulse durations, with amplitudes significantly exceeding the algebraic sum of individual pulses (Table S2), thereby mimicking the supralinear integration properties of neuronal dendrites. The simultaneous demonstration of synaptic plasticity and dendritic integration at the single-molecule scale establishes a new paradigm for energy-efficient neuromorphic device design.

To induce the transition from short-term to long-term plasticity (Fig. 2e and Fig. S18), we implemented paired-pulse facilitation (PPF) by applying consecutive double-pulse stimulation. The device achieved a maximum PPF index of ~307.99% at 10 ms intervals, with an exponential decay observed as the intervals increased to 300 ms. With twelve consecutive pulses, the device exhibited progressive enhancement of EPSC conductance states while maintaining frequency sensitivity (Fig. S19), exhibiting biological synapse-like multilevel plasticity and frequency-dependent potentiation similar to biological systems. Control of pulse intervals and durations enabled the identification of more than 10 distinct conductance states (including baseline; Fig. 2f, Fig S20 and Table S3)[45], highlighting the potential of this single-molecule device for programmable neuromorphic computing and multilevel memory applications.

Expanding these findings, we emulated the "learn-forget-relearn" behavior using the single **MeO-TBT** synapse (Fig. S21 and Table S4). The initial learning phase required six pulses to achieve conductance saturation, whereas relearning attained the same state with only three pulses (a 50% increase in learning efficiency). Notably, conductance retention improved from 21.15% to 45.57% during short-term forgetting (10 ms intervals) and from 4.18% to 7.61% in long-term forgetting (400 ms intervals). Beyond implementing spike-timing-dependent plasticity (STDP)[46], the device exhibited memory reconsolidation through cumulative ion migration, establishing a platform for autonomous neuromorphic computing systems.

Associative learning and recognition using a single-molecule neuromorphic device

To demonstrate the potential of neuromorphic computing with the single-molecule device, we emulated associative learning behavior under the synergistic stimulation of V_G and V_B pulses. The single-molecule conductance curve (Fig. 3a, for more details, see Fig. S22 and the corresponding caption), together with the two-dimensional histogram compiled from 134 individual traces (Fig. 3b and Fig. S23), conclusively demonstrates that our single-molecule device can implement classical Pavlovian conditioning[47]. Electrical pulse sequence 1 was used as the conditioned stimulus (CS),

emulating the scenario in which a dog hears a bell without response. Sequence 2 served as the unconditioned stimulus (UCS), representing the dog's response upon seeing food. The device was trained by simultaneously applying both sequences, mimicking the experience of the dog hearing the bell while seeing food. Finally, when sequence 1 was applied again to emulate the dog hearing the bell once more, thus the device exhibited a response. This indicates that the device is capable of emulating associative learning behavior after pre-training.

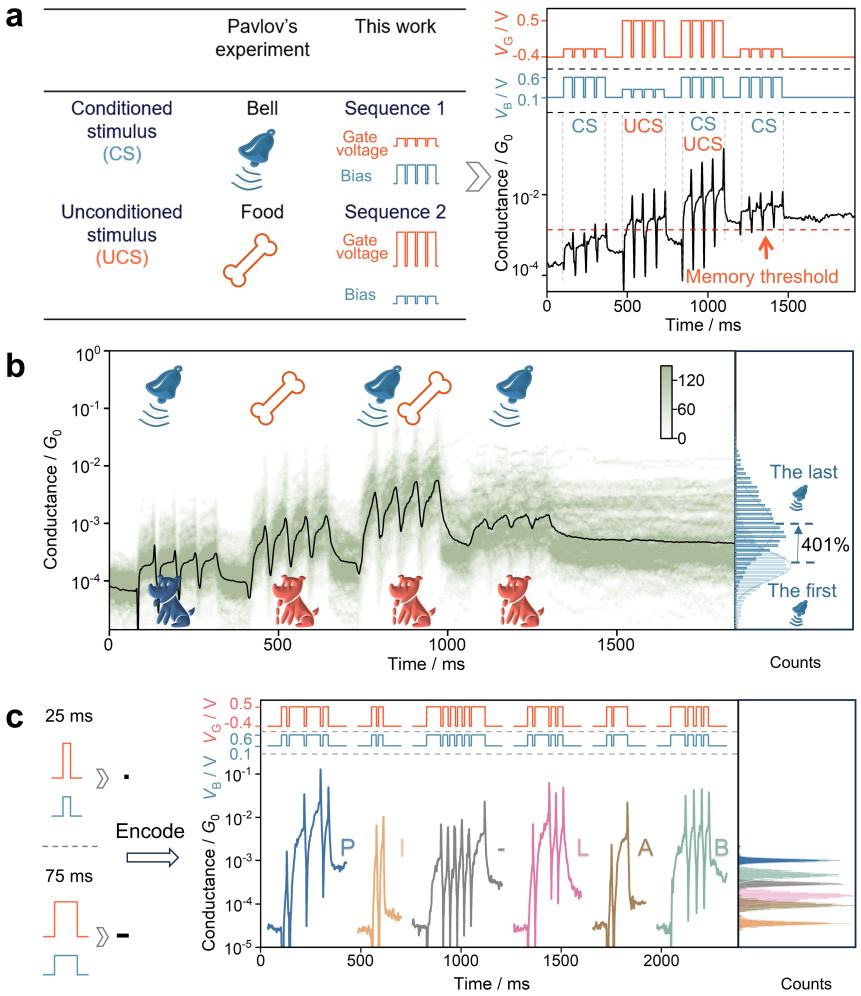


Fig. 3 Associative learning and Morse code recognition. a, b, Mimicking Pavlov's experiment using a single-molecule device. A representative single-molecule conductance curve (right panel of Fig. a) and statistical results from 134 traces (Fig. b) demonstrate the emulation of Pavlov's experiment. The conductance was enhanced by approximately 401% after training (see histograms in the right column). **c,** Morse code decoding of the six characters of "PI-LAB" was achieved with tunable pulse durations (V_G = 0.5 V, V_B = 0.6 V, t_p= 50 ms, Δt = 10 ms): 25 ms for "." and 75 ms for "-" with distinguishable output conductance states, as indicated in the histograms at right.

Morse code recognition was further performed to demonstrate the information processing capabilities of this single-molecule neuromorphic device[48]. Here, excitatory postsynaptic conductance (EPSC) values generated by 25 ms and 75 ms electrical pulses were used to encode the dot (".") and dash ("-") signals, respectively (Fig. 3c and Figs. S24-S25). As shown, the name of our laboratory "PI-LAB" can be represented using low and high EPSC amplitudes through temporally coded pulse input signals. Importantly, comparative analysis of the steady-state conductance after pulse termination reveals distinct differences corresponding to the encoded Morse code patterns. This clear conductance differentiation demonstrates the intrinsic capability of the single-molecule device for temporal pattern recognition. Furthermore, key feature parameters extracted from the conductance data of this single-molecule neuromorphic device were used to construct an artificial spiking neural network (SNN) model (Fig. S26) for the task of MNIST handwritten digit recognition[49,50]. Experimental results show that this model achieves a classification accuracy of 97.4% and notably exhibits human-like cognitive confusion when handling blurred images (accuracy of 96%), highlighting the potential of single-molecule devices in image and voice processing applications.

Mechanism of the single-molecule neuromorphic device

To elucidate the operational mechanism of single-molecule neuromorphic devices, we performed large-scale force-field molecular dynamics (FFMD) simulations to investigate electric-field-driven ionic migration of TBA^+ and PF_6^- (Fig. 4a and Movie S1)[51]. Validation of the force field was achieved by simulating TBA^+ and PF_6^- self-diffusion in 0.2 M propylene carbonate solution (Fig. S27a). The simulated self-diffusivity of TBA^+ and PF_6^- is 3.83×10^{-10} $m^2 \cdot s^{-1}$ and 4.74×10^{-10} $m^2 \cdot s^{-1}$, respectively, consistent with experimental pulsed field gradient-NMR measurements. (Figs. S27b, S28)[52]. Under an applied electric field (positive *X*-axis as gate voltage and positive *Y*-axis as bias voltage), TBA^+ ions migrated along the field direction, while PF_6^- ions moved oppositely, with preferential accumulation near the **MeO-TBT** bottom (Fig. S29). Ion mobilities were quantified as $(5.92 \pm 3.37) \times 10^{-5}$ $cm^2 \cdot V^{-1} \cdot s^{-1}$ (TBA^+) and $(6.96 \pm 2.98) \times 10^{-4}$ $cm^2 \cdot V^{-1} \cdot s^{-1}$ (PF_6^-). FFMD simulations further revealed three distinct states: coupling (**State I**) and decoupling (**States II** and **III**) between **MeO-TBT** and TBA^+.

To elucidate the nature of interactions between **MeO-TBT** and the ammonium cations, we constructed models representing the interaction of **MeO-TBT** with one and two ammonium cations, optimizing them to obtain the lowest energy configurations (Fig. 4b and Fig. S30). In the absence of molecule–ion interactions, the O–S distance measures 2.7 Å and the S–C1–C2–C3 dihedral angle is 15° on both sides of the molecule (Fig. S31a). Applying a weak electric field (2 a.u.) along the S–S direction results in O–S distances of 2.7 Å and dihedral angles of 10° and 19° (Fig. S31b), respectively. When the electric field strength is increased to 20 a.u., positive ions migrate closer to the molecule. As a result, both the O–S distance and the dihedral angle increase, reaching values of 2.80 Å and 28° (Fig. S31c),

respectively, with consistent values observed on both sides. The sulfur and oxygen atoms in the **MeO-TBT** molecule electrostatically interact with the hydrogen atoms from the cations of TBA^+, with distances of 2.97 and 2.41 Å, respectively. In addition to these electrostatic interactions, there is a potential electrostatic attraction between the hydrogen atoms and the conjugated plane of **MeO-TBT**. To clarify the changes in conductance of **MeO-TBT** during the coupling and decoupling processes with ammonium cations, we calculated the transmission spectra on **state I**, **state II**, and **state III** corresponding to Figs. 2a and 4a (Fig. 4b). The results indicate that when **MeO-TBT** is in a coupled state with two cations, the transmittance is at its lowest, gradually increasing as the decoupling proceeds. These observations correlate well with the conductance changes observed during electric pulse application in our experiments. Our calculations yield a cumulative energy consumption profile for single TBA^+ ion migration around **MeO-TBT** (Fig. 4c), showing an average energy consumption of ~2.1 aJ. This theoretical value agrees well with the experimental energy consumption range of ~2.8 aJ per operation. Together, these results provide strong theoretical evidence for the ion-migration-mediated molecule-ion dynamic coupling mechanism.

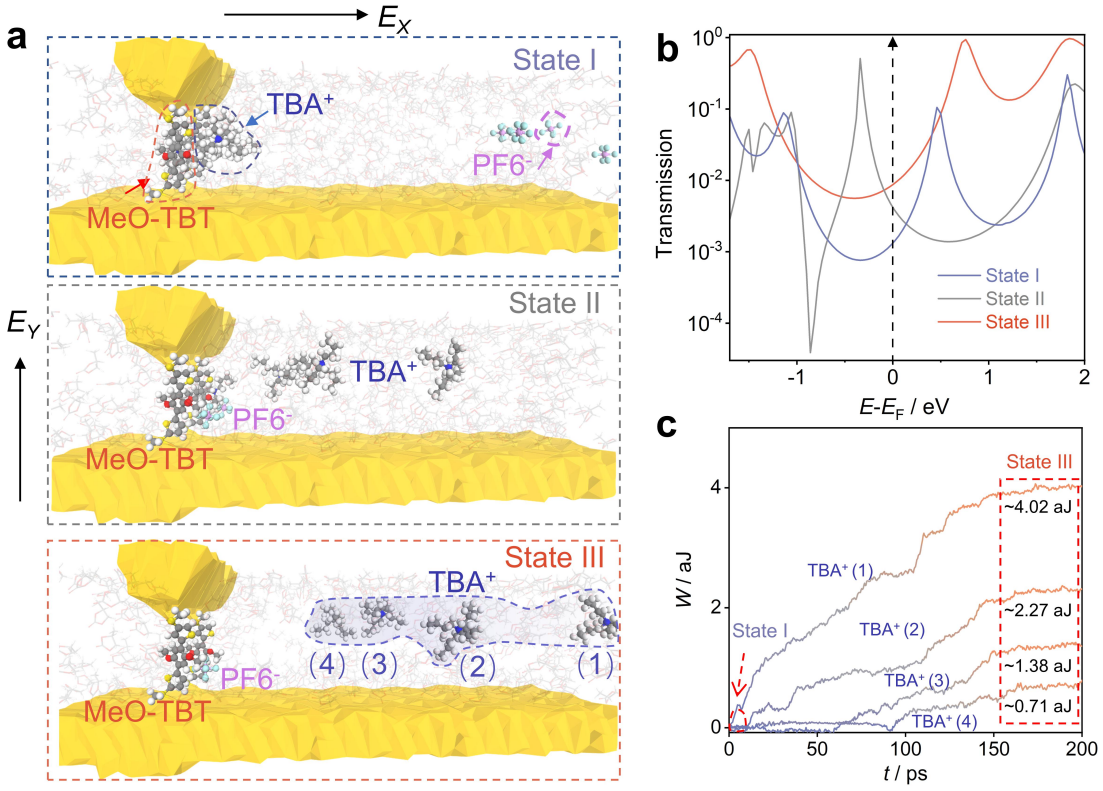


Fig. 4 Mechanism of multiple conductance states in single-molecule neuromorphic devices. a, Simulated ion migration under an external electric field (positive *X*- and *Y*-axis components) using nonequilibrium molecular dynamics (MD). **b,** Transmission spectra calculations for the single-molecule junction in **state I**, **state II** and **state III** (corresponding to Fig. 2a). To simplify computations while preserving key chemical characteristics, we substituted tetrabutylammonium with

tetramethylammonium cations in the model. **c,** Theoretical time-dependent cumulative energy profile for TBA^+ migration around **MeO-TBT**.

To further verify the operation mechanism of the single-molecule neuromorphic device, we conducted control experiments on the target molecule and the electrolyte. The results indicated that the I-V_G curves of 5,5'-(2,5-diethyl-1,4-phenylene) bis(2-(methylthio)thiophene) (**Et-TBT**) without the S-O non-covalent interactions showed a much smaller hysteresis area, while the I-V_B curves exhibited almost no hysteresis (Figs. S32 and S33). This suggests that the memory function of the device is closely related to the non-covalent S-O interactions in **MeO-TBT**. Control experiments using different electrolytes (Fig. 2d and Figs. S7-S10, S34-S36) revealed that devices containing ammonium ions exhibited significant hysteresis effects in both I-V_G and I-V_B tests, whereas the control group exhibited negligible hysteresis, confirming the critical role of ammonium ions in achieving memory functionality. Furthermore, it was observed that the lower-mobility tetrabutylammonium cations generated a larger hysteresis area in the I-V_G tests compared to tetraethylammonium cations (Table S5), which aligned perfectly with theoretical predictions. This indicated that restricted ionic movement effectively prolonged memory retention duration. In summary, both the theoretical and experimental findings demonstrate that a single molecule with S-O non-covalent interactions can endow the device with a history-dependent memory function through interactions with surrounding ammonium cations.

Discussion

In conclusion, we demonstrate a single-molecule neuromorphic device by fine tuning of the molecule-ion coupling via electrochemical gating. This bio-inspired single-molecule electrochemical synapse integrates synaptic and dendritic functionalities, achieving ultra-low energy consumption of ~2.8 aJ/operation. Through programmable molecule-cation electrostatic interactions, this device realizes biomimetic emulation of neural plasticity transitions from short-term (PPF index of about 307.99%) to long-term memory featuring over 10 distinct conductance states, fulfilling the associative learning of Pavlovian experiment and pattern recognition of Morse code. Our findings provide the first experimental demonstration of neuromorphic devices at the single-molecule scale, which offer unique potential for energy-sustainable artificial intelligence.

Methods

Materials

MeO-TBT and **Et-TBT** were synthesized according to our previous report[40]. ^1H NMR and ^{13}C NMR spectra were measured with Fourier 300 MHz. Mass spectra were collected on a Bruker Solarix-XR high-resolution mass spectrometer.

Conductance measurements

Conductance measurements were performed using a home-built EC-STMBJ system. The distance between the gold tip electrode and the gold substrate electrode was adjusted using a stepper motor and a piezoelectric ceramic. When a nanogap was formed between the two electrodes, the sample molecule entered the gap, connecting to the substrate and tip electrodes via methylthio groups to form a single-molecule junction. The tip and substrate electrodes were repeatedly brought together and separated to perform multiple cycles of break junction[53]. A platinum electrode served as the counter electrode, and an Ag/AgCl electrode acted as the reference electrode while recording the distance between the gold electrodes and the conductance of the single-molecule junction under various potential conditions. To minimize interference from leakage currents under electrochemical conditions, the gold tips obtained through electrochemical etching were encapsulated with black wax. Finally, the dynamic break junction process and the electrochemical behavior of the single-molecule junctions were analyzed using a custom-developed Python program to process large volumes of experimental data. We conducted measurements of the single-molecule conductance of 0.5 mM **MeO-TBT** in a propylene carbonate (PC) solution containing 0.1 M tetrabutylammonium hexafluorophosphate ($TBAPF_6$) as the electrolyte at electrode potentials within the non-Faradaic region (gate voltage V_G ranging from –0.4 V to 0.5 V) under a bias voltage of 0.1 V (Figs. S2-6).

To optimize the memory characteristics of the device, we optimized the concentration used in the tests as well as the solvents[32]. First, we adjusted the electrolyte concentration and compared the test results of $TBAPF_6$ at concentrations of 0.05 M, 0.1 M, and 0.2 M (Figs. S7-9). The results show that as the electrolyte concentration increases, the on/off ratio of the I-V_G and I-V_B hysteresis curves also increases. This indicates that electrolyte concentration plays a crucial role in adjusting the memory characteristics of the device. However, when the concentration exceeds 0.2 M, partial precipitation occurs due to its limited solubility in the PC solvent. Therefore, 0.2 M was selected as the optimal concentration for subsequent experimental investigations. Next, we further explored the impact of the solvent on the device memory characteristics (Figs. S10 and S11). On this basis, we compared the I-V_G and I-V_B curves of the device in PC, acetonitrile, and ionic liquid (1-hexyl-3-methylimidazolium hexafluorophosphate) solutions, respectively. The experimental data demonstrate that the hysteresis effect is most pronounced in PC, which was therefore selected as the optimized solvent for subsequent studies. Our findings reveal that the single-molecule synaptic transistor based on **MeO-TBT** exhibits relatively good memory characteristics in a PC solution of 0.2 M $TBAPF_6$.

The characterization of current-voltage (I-V_B) curves is conducted in a “hover” mode, where the conductance changes between the working electrodes are monitored under set bias voltage and potential conditions. The transition into hover mode is determined by built-in judgment logic within our custom-developed testing software. When sampling points within a preset conductance range (based on the statistical conductance range of the target molecule) are detected and exceed a certain threshold, this indicates that the “hover” mode has been achieved, signaling the formation of a

single-molecule junction. At this point, the piezoelectric ceramic ceases movement, and the I-V_B curve measurement is performed at a scanning speed of 10 V/s. After testing, the extensive I-V_B curves obtained are subjected to statistical analysis using laboratory-developed Python software.

The data for current-gate voltage (I-V_G) curves is derived from conductance-gate voltage curves (G-V_G) using the formula $I = G*V$. The characterization of conductance-gate voltage curves is performed in hover mode. In this mode, the potential is swept forward and backward within the potential range of –0.4 to 0.5 V, with a scanning speed of 2 V/s. After testing, a large number of G-V_G curves are subjected to statistical analysis using laboratory-developed Python software. Finally, the I-V_G curves are obtained by converting the data using the established formula.

The data for current-gate voltage (I-V_G) curves is derived from conductance-gate voltage curves (G-V_G) using the formula $I = G*V$. The characterization of conductance-gate voltage curves is performed in hover mode. In this mode, the potential is swept forward and backward within the potential range of –0.4 to 0.5 V, with a scanning speed of 2 V/s. After testing, a large number of G-V_G curves are subjected to statistical analysis using laboratory-developed Python software. Finally, the I-V_G curves are obtained by converting the data using the established formula.

Mimicking synaptic plasticity through a single-molecule device

In our study, we emulated synaptic plasticity by applying designed pulse sequences in a “hover” mode, which allows for the application of various electrical pulse sequences to emulate synaptic behavior and monitor conductance changes. We verified that the EC-STMBJ setup can achieve stable hovering (Fig. S12). we separately applied the separate gate voltage pulse, the separate bias pulse, and combined gate and bias voltage pulses to the device in hover mode (Figs. S15-21). Depending on the inputted sequences, the duration of a single hover session ranges from 200 to 2300 ms. After testing, the results are analyzed using laboratory-developed Python software.

Handwritten digit recognition simulation

The presented spiking neural network (SNN) incorporates dual-exponential synaptic conductance dynamics[49,50], establishing a biologically interpretable hierarchical processing architecture (Fig. S26a). The input layer receives 28 × 28 pixel grayscale images, which undergo temporal encoding through a Poisson spike generator governed by the following stochastic process:

$$s_{ij(t)} \sim Bernoulli\left(x_{ij}\right), \forall\, t = \left\{1, 2, \ldots, \mathrm{T}\right\} \tag{1}$$

Where $x_{ij} \in [0, 1]$ denotes normalized pixel intensity values and T=10 ms specifies the temporal window duration. This encoding mechanism probabilistically transforms spatial luminance information into temporally distributed spike trains, maintaining intensity-proportional firing rates across the input population.

The encoded spatiotemporal spike patterns propagate through a fully-connected network with bifurcated synaptic conductance pathways. The first synaptic layer implements feature projection through dimensional reduction from 784 input channels to 128 latent features:

$$h_{1(t)} = W_{1s(t)} + b_1 \tag{2}$$

where $W_1 \in R^{\{128\times784\}}$ represents the trainable weight matrix. Subsequent spike generation is governed by dual-exponential neuronal dynamics.

$$i_{\text{fast}}^{t} = \alpha i_{\text{fast}}^{t-1} + h_{1(t)} \tag{3}$$

$$i_{\text{slow}}^{t} = \beta i_{\text{slow}}^{t-1} + h_{1(t)} \tag{4}$$

$$v^{t} = v^{t-1} + \left(i_{\text{fast}}^{t} - i_{\text{slow}}^{t}\right) \tag{5}$$

The decay coefficients are defined as:

$$\alpha = \exp\left(-\frac{1}{\tau_3}\right) \tag{6}$$

$$\beta = \exp\left(-\frac{1}{\tau_4}\right) \tag{7}$$

characterizing fast and slow temporal integration constants. A firing threshold mechanism triggers spike emission when $v(t) \geq \theta_{\text{th}} = 1\,mV$, followed by instantaneous membrane potential reset to baseline.

The secondary synaptic layer performs categorical projection through dimensionality reduction from 128 hidden features to 10 output classes:

$$h_{2(t)} = W_{2s_{1(t)}} + b_2 \tag{8}$$

Where $W_2 \in R^{\{10\times128\}}$ denotes the class-specific weight matrix. The final classification probabilities emerge through temporal integration of output spikes:

$$p_c = \left(\frac{1}{T}\right)\Sigma_{\{t=1\}}^{T} s_2^{c(t)} \tag{9}$$

This architecture leverages dual-exponential differentiation mechanisms for temporal filtering, where the antagonistic interaction between fast (τ_3) and slow (τ_4) currents enhances spatiotemporal pattern discrimination. Network parameters are

optimized via spatio-temporal backpropagation through time (BPTT) algorithm, supervised by cross-entropy loss minimization:

$$L = -\sum_{c=0}^{9} y_c \log(p_c) \tag{10}$$

Through the proposed biologically plausible training paradigm, the model achieved progressive optimization of the objective function, attaining a final training loss of $L_{\text{train}} = 1.626$ (Fig. S26b). This minimization process demonstrated strict adherence to neuromorphic learning principles, exhibiting a smooth convergence trajectory, stable parameter updates, and effective gradient propagation. The optimized network achieved peak classification accuracies of 97.4% on the validation set (Fig. S26c) and 96.9% on the hold-out test set (Fig. S26d), demonstrating a minimal 0.5% performance deviation indicative of robust generalization.

Dynamic calculation

The force-field molecular dynamics (MD) simulations were performed using the Materials Studio package (Acelrys Software)[51]. The interatomic interactions were described by the condensed-phase-optimized molecular potentials for atomistic simulation studies (COMPASS) force field, and the electrostatic energy was calculated by the Ewald & Group summation method. The Ewald & Group summation method has an Ewald accuracy of 10^{-5} kcal·mol^{-1} when used for calculating electrostatic potential energy. The periodic boundary conditions were set in all three directions. The electrostatic interactions were computed using Ewald methods. The velocity Verlet algorithm was used to integrate the Newton's equations of motion with a time step of 1 *f*s. A cutoff radius of 18.5 Å was assumed for Lennard-Jones interaction potential calculation. The simulated temperature was controlled by a Nosé thermostat.

The self-molecular diffusivities were obtained from equilibrium MD simulations. The size of box is 45.0 × 45.0 × 45.0 Å^3, which contains 600 PC, 10 TBA^+ and 10 PF_6^- molecules. The box was firstly optimized by the geometry optimization using force field. Then the *NpT* ensemble, *i.e.* the numbers of particles (*N*), pressure (*p*) and temperature (*T*) are kept as constants, were performed for 100 *p*s in 100000 steps for systems after the systems are equilibrated at 298 K. After equilibrium under *NpT* ensemble, dynamics processes in the *NVT* ensemble, *i.e.* the numbers of particles (*N*), volume (*V*) and temperature (*T*) are kept as constants, were performed for 200 ps in 200000 steps for systems after the systems are equilibrated at 298 K. The mean square displacement (*MSD*) of ions is shown in Fig. S25. The slope of *MSD* as a function of time was used to determine the self-diffusivity following Einstein relation.

$$MSD(\tau) = 2nD\tau + b \tag{11}$$

where *MSD* is the mean squared displacement, *n* is the dimension of framework (*n* = 3 for 3D frameworks), *D* is the diffusion coefficient, τ is the time, and *b* is the thermal factor arising from atomic vibrations.

The ions migration under the external electric field were obtained from non-equilibrium MD simulations. The size of box is 26.1 × 90.4 × 31.3 $Å^3$, which contains 340 PC, 4 TBA^+, 4 PF_6^- and 2 molecules linked by the Au tip and Au substrate. The box was firstly optimized by the geometry optimization using force field. Then the *NVT* ensemble were performed for 200 ps in 200000 steps for systems after the systems are equilibrated at 298 K. The external electric field (E_x = + 0.28 V/Å and E_y = + 0.28 V/Å) was applied under *NVT* ensemble, the *NVT* ensemble were performed for 200 *p*s in 200000 steps. The ionic mobility of TBA^+ is defined by the ratio between distance between molecular lock and TBA^+ to simulation time (200 *p*s). The ionic mobility of PF_6^- is defined by the ratio between distance between molecular lock and PF_6^- to simulation time (arriving to the bottom of molecular lock, the started time of platform in Fig. S29).

To support the accuracy of our theoretical simulations, we conducted NMR pulsed gradient experiments (Fig. S28). Theoretical calculations indicated that PF_6^- anions diffuse faster than TBA^+ cations in PC solution. Therefore, we used NMR pulsed gradient experiments to measure the diffusion coefficients of both anions and cations in the same solution[52]. The NMR results showed that the diffusion coefficient for PF_6^- is 4.850×10^{-10} m^2/s, while for TBA^+ is 3.048×10^{-10} m^2/s. Theoretically, the diffusion coefficient for PF_6^- is 4.740×10^{-10} m^2/s, while for TBA^+ is 3.830×10^{-10} m^2/s. These experimental results align well with the theoretical simulation values, providing strong support for the accuracy of the kinetic simulations.

To elucidate the nature of interactions between **MeO-TBT** and the ammonium cation, we constructed models representing the interaction of **MeO-TBT** with ammonium cations, optimizing them to obtain the lowest energy configurations. To clarify the changes in conductance of **MeO-TBT** during the coupling and decoupling processes with ammonium cations, we conducted transmission spectra calculations on the states of **MeO-TBT**, **MeO-TBT** coupled with one ammonium cation, and **MeO-TBT** coupled with two ammonium cations.

Thermodynamic calculation

The individual molecular structures including **MeO-TBT**, PF_6^- and $N(CH_3)_4^+$ were constructed and optimized with Gaussian 09 software under B3LYP functionals and 6-311G**basis set (Fig. S30)[36]. To explore the interaction between **MeO-TBT** and positively charged ions, the $N(CH_3)_4^+$ ions were placed at a distance of 5 Å from the S-O interaction for structural optimization, and a 20 a.u. electric field was applied in the *y*-direction to simulate the experimental gate electric field. This optimization process was conducted under identical functionals and basis set with DFT-D3 dispersion correction. We then used the fully relaxed structures for the single point energy determination and calculated under m062x functionals and 6-311+G** with applied electric field and frequency calculation.

Transmission calculation

To construct the single-molecule devices, the gold electrodes were constructed with 9*9*6 gold atoms and anchors with the target molecule with the pyramid shaped gold

atoms at the top. The single-molecule devices were constructed with QuantumATK U-2022.12 software and optimized with PBE-GGA functional and Double-ζ Polarized (DZP) basis set (Double-ζ, DZ for gold atoms). The k-point was set as 4*4*150. To calculate the transmission spectrum, the Non-equilibrium Green Function and Landauer formula. The current flow through the molecular junction is defined as:

$$I = (2\frac{e}{h})\int_{-\infty}^{\infty} dET(E)[f_{\text{left}}(E) - f_{\text{right}}(E)] \quad (12)$$

where e is the electronic charge, h is Planck's constant and $T(E)$ is the transmission coefficient for electrons passing from one electrode to another.

References

1 Maslej, N. et al., Artificial intelligence index report 2025. (Stanford University: Stanford, CA, USA, 2025). https://hai.stanford.edu/ai-index/2025-ai-index-report

2 AI hardware has an energy problem. *Nat. Electron.* **6**, 463-463 (2023).

3 Gkoupidenis, P. *et al.* Organic mixed conductors for bioinspired electronics. *Nat. Rev. Mater.* **9**, 134-149 (2024).

4 Harikesh, P. C. *et al.* Ion-tunable antiambipolarity in mixed ion–electron conducting polymers enables biorealistic organic electrochemical neurons. *Nat. Mater.* **22**, 242-248 (2023).

5 Sangwan, V. K. & Hersam, M. C. Neuromorphic nanoelectronic materials. *Nat. Nanotechnol.* **15**, 517-528 (2020).

6 Wang, S. *et al.* An organic electrochemical transistor for multi-modal sensing, memory and processing. *Nat. Electron.* **6**, 281-291 (2023).

7 Zhou, T. *et al.* Large-scale neuromorphic optoelectronic computing with a reconfigurable diffractive processing unit. *Nat. Photon.* **15**, 367-373 (2021).

8 Liu, R. *et al.* Hardware-feasible and efficient n-type organic neuromorphic signal recognition via reservoir computing. *Adv. Mater.* **37**, 2409258 (2025).

9 Baek, E. *et al.* Neuromorphic dendritic network computation with silent synapses for visual motion perception. *Nat. Electron.* **7**, 454-465 (2024).

10 Wang, W. *et al.* Neuromorphic sensorimotor loop embodied by monolithically integrated, low-voltage, soft e-skin. *Science* **380**, 735-742 (2023).

11 Strukov, D. B., Snider, G. S., Stewart, D. R. & Williams, R. S. The missing memristor found. *Nature* **453**, 80-83 (2008).

12 Prezioso, M. *et al.* Training and operation of an integrated neuromorphic network based on metal-oxide memristors. *Nature* **521**, 61-64 (2015).

13 Pazos, S. *et al.* Synaptic and neural behaviours in a standard silicon transistor. *Nature* **640**, 69-76 (2025).

14 Sharma, D. *et al.* Linear symmetric self-selecting 14-bit kinetic molecular memristors. *Nature* **633**, 560-566 (2024).

15 Siddique, R., Eftimie, M. & Banad, Y. M. A comparative analysis of neuromorphic neuron circuits for enhanced power efficiency and spiking frequency in 22nm CMOS technology. *2024 IEEE 67th International Midwest Symposium on Circuits and Systems (MWSCAS)* (2024), pp. 1096-1100.

16 Galperin, M., Ratner, M. A., Nitzan, A. & Troisi, A. Nuclear coupling and polarization in molecular transport junctions: beyond tunneling to function. *Science* **319**, 1056-1060 (2008).

17 Leary, E. *et al.* Incorporating single molecules into electrical circuits. The role of the chemical anchoring group. *Chem. Soc. Rev.* **44**, 920-942 (2015).

18 Shaik, S., Ramanan, R., Danovich, D. & Mandal, D. Structure and reactivity/selectivity control by oriented-external electric fields. *Chem. Soc. Rev.* **47**, 5125-5145 (2018).

19 Su, T. A., Neupane, M., Steigerwald, M. L., Venkataraman, L. & Nuckolls, C. Chemical principles of single-molecule electronics. *Nat. Rev. Mater.* **1**, 16002 (2016).

20 Xin, N. *et al.* Concepts in the design and engineering of single-molecule electronic devices. *Nat. Rev. Phys.* **1**, 211-230 (2019).

21 Bai, J., Li, X., Zhu, Z., Zheng, Y. & Hong, W. Single-Molecule Electrochemical Transistors. *Adv. Mater.* **33**, 2005883 (2021).

22 Ciampi, S., Darwish, N., Aitken, H. M., Díez-Pérez, I. & Coote, M. L. Harnessing electrostatic catalysis in single molecule, electrochemical and chemical systems: a rapidly growing experimental tool box. *Chem. Soc. Rev.* **47**, 5146-5164 (2018).

23 Yan, X. *et al.* Moiré synaptic transistor with room-temperature neuromorphic functionality. *Nature* **624**, 551-556 (2023).

24 Wang, Y. *et al.* Dynamic molecular switches with hysteretic negative differential conductance emulating synaptic behaviour. *Nat. Mater.* **21**, 1403-1411 (2022).

25 Zhang, Y. *et al.* An artificial synapse based on molecular junctions. *Nat. Commun.* **14**, 247 (2023).

26 Li, J. *et al.* Room-temperature logic-in-memory operations in single-metallofullerene devices. *Nat. Mater.* **21**, 917-923 (2022).

27 Zhang, K. *et al.* A Gd@C82 single-molecule electret. *Nat. Nanotechnol.* **15**, 1019-1024 (2020).

28 Li, J. *et al.* In-situ electro-responsive through-space coupling enabling foldamers as volatile memory elements. *Nat. Commun.* **14**, 6250 (2023).

29 Diez-Perez, I. *et al.* Controlling single-molecule conductance through lateral coupling of π orbitals. *Nat. Nanotechnol.* **6**, 226-231 (2011).

30 Tang, Y. *et al.* Electric field-Induced assembly in single-stacking terphenyl

junctions. *J. Am. Chem. Soc.* **142**, 19101-19109 (2020).

31 Venkataraman, L., Klare, J. E., Nuckolls, C., Hybertsen, M. S. & Steigerwald, M. L. Dependence of single-molecule junction conductance on molecular conformation. *Nature* **442**, 904-907 (2006).

32 Xiong, T. *et al.* Neuromorphic functions with a polyelectrolyte-confined fluidic memristor. *Science* **379**, 156-161 (2023).

33 Robin, P. *et al.* Long-term memory and synapse-like dynamics in two-dimensional nanofluidic channels. *Science* **379**, 161-167 (2023).

34 Fuller, E. J. *et al.* Parallel programming of an ionic floating-gate memory array for scalable neuromorphic computing. *Science* **364**, 570-574 (2019).

35 Aragonès, A. C. *et al.* Electrostatic catalysis of a Diels–Alder reaction. *Nature* **531**, 88-91 (2016).

36 Bai, J. *et al.* Anti-resonance features of destructive quantum interference in single-molecule thiophene junctions achieved by electrochemical gating. *Nat. Mater.* **18**, 364-369 (2019).

37 Chang, S. *et al.* Tunnelling readout of hydrogen-bonding-based recognition. *Nat. Nanotechnol.* **4**, 297-301 (2009).

38 Haiss, W. *et al.* Precision control of single-molecule electrical junctions. *Nature Materials* **5**, 995-1002 (2006).

39 Reddy, H. *et al.* Determining plasmonic hot-carrier energy distributions via single-molecule transport measurements. *Science* **369**, 423-426 (2020).

40 Naghibi, S. *et al.* Redox-addressable single-molecule junctions incorporating a persistent organic radical. *Angew. Chem. Int. Ed.* **61**, e202116985 (2022).

41 Zhang, H. *et al.* Dual modulation of single molecule conductance via tuning side chains and electric field with conjugated molecules entailing intramolecular O•••S interactions. *Adv. Sci.* **9**, 2105667 (2022).

42 Kim, S. J. *et al.* Linearly programmable two-dimensional halide perovskite memristor arrays for neuromorphic computing. *Nat. Nanotechnol.* **20**, 83-92 (2025).

43 2022 International Roadmap for Devices and Systems (Tech. Rep., IEEE, 2022); https://irds.ieee.org.

44 Kam, H., Liu, T. J. K., Stojanović, V., Marković, D. & Alon, E. Design, optimization, and scaling of MEM relays for ultra-low-power digital logic. *IEEE Trans. Electron Devices* **58**, 236-250 (2011).

45 Weilenmann, C. *et al.* Single neuromorphic memristor closely emulates multiple synaptic mechanisms for energy efficient neural networks. *Nat. Commun.* **15**, 6898, (2024).

46 Larimer, P. & Strowbridge, B. W. Timing is everything. *Nature* **448**, 652-653 (2007).

47 Ji, X. *et al.* Mimicking associative learning using an ion-trapping non-volatile synaptic organic electrochemical transistor. *Nat. Commun.* **12**, 2480 (2021).

48 Kim, H., Oh, S., Choo, H., Kang, D.-H. & Park, J.-H. Tactile neuromorphic system: convergence of triboelectric polymer sensor and ferroelectric polymer synapse. *ACS Nano* **17**, 17332-17341 (2023).

49 LeCun, Y., Bengio, Y. & Hinton, G. Deep learning. *Nature* **521**, 436-444 (2015).

50 Yao, P. *et al.* Fully hardware-implemented memristor convolutional neural network. *Nature* **577**, 641-646 (2020).

51 Gao, M. *et al.* Imaging spatiotemporal evolution of molecules and active sites in zeolite catalyst during methanol-to-olefins reaction. *Nat. Commun.* **11**, 3641 (2020).

52 Ferrage, F., Zoonens, M., Warschawski, D. E., Popot, J.-L. & Bodenhausen, G. Slow diffusion of macromolecular assemblies by a new pulsed field gradient NMR method. *J. Am. Chem. Soc.* **125**, 2541-2545 (2003).

53 Li, X. *et al.* Supramolecular transistors with quantum interference effect. *J. Am. Chem. Soc.* **145**, 21679-21686 (2023).

Data availability All data that support the findings of this study are available from the corresponding author upon reasonable request.

Acknowledgments This work was supported by the National Natural Science Foundation of China (Nos. 22325303, 21933012, 22250003, 22173075, 22303071), the National Key Research and Development Program of China (2024YFA1208103), the Fujian Provincial Department of Science and Technology (2023H6002), and the Fundamental Research Funds for the Central Universities (Nos. 20720220020, 20720200068, 20720240040), the Open Research Fund of Key Laboratory of Precision and Intelligent Chemistry.

Author contributions W.H., D.Z. and J.L. supervised the project. W.H., D.Z., J.L., and H.Z. conceived the concept and designed the experiments. H.Z. synthesized the test molecules with the support by W.S. and L.C.; H.Z. performed the measurements with the support by Y.J.; H.Z. conducted the data analysis with the support by J.W., B.Z., W.X., C.Y., X.L., J.B., J.L., X.Z., J.S., Y.Z., G.Z.; J.Y. and M.G. conducted the theoretical calculations with the help of Y.Z.; W.H., D.Z., J.L. and H.Z. prepared the manuscript with input from other authors.

Competing interests The authors declare no competing interests.

Supplementary Files

This is a list of supplementary files associated with this preprint. Click to download.

- SinglemoleculeneuromorphicdeviceSI.docx
- MovieS11.mp4